

UCLA

UCLA Previously Published Works

Title

Improved Sorption-Enhanced Steam Methane Reforming via Calcium Oxide-Based Sorbents with Targeted Morphology

Permalink

<https://escholarship.org/uc/item/4q70s527>

Journal

Energy Technology, 7(3)

ISSN

2194-4288

Authors

Alshafei, Faisal H
Minardi, Luke T
Rosales, Derrick
[et al.](#)

Publication Date

2019-03-01

DOI

10.1002/ente.201800807

Peer reviewed

Improved Sorption-Enhanced Steam Methane Reforming via Calcium Oxide–Based Sorbents with Targeted Morphology

Faisal H. Alshafei, Luke T. Minardi, Derrick Rosales, Gen Chen, and Dante A. Simonetti*

Calcium oxide (CaO)-based sorbents for sorption enhanced steam methane reforming (SE-SMR) that achieve stoichiometric capacity are synthesized via thermal and electrospinning methods. Small CaO crystallites (39 nm) and macroporous intrafiber networks imparted by electrospinning lead to stoichiometric capacities ($0.79 \text{ g}_{\text{CO}_2} \text{ g}_{\text{sorbent}}^{-1}$) and uptake kinetics (first order rate constant, $k = 8.9 \times 10^{-4} \pm 1.8 \times 10^{-5} \text{ cm}^4 \text{ mol}^{-1} \text{ s}^{-1}$) at 873 K that are superior to CaO derived from thermal syntheses ($0.05\text{--}0.7 \text{ g}_{\text{CO}_2} \text{ g}_{\text{sorbent}}^{-1}$ and $k < 5.0 \times 10^{-4} \pm 2.5 \times 10^{-6} \text{ cm}^4 \text{ mol}^{-1} \text{ s}^{-1}$). Al-doped electrospun CaO samples (Al:Ca ratios of 3:10, 1:10 and 2:10) also exhibit high sorption capacities ($0.35\text{--}0.74 \text{ g}_{\text{CO}_2} \text{ g}_{\text{sorbent}}^{-1}$ at 873 K) and are stable over multiple reaction-regeneration cycles (<5% loss in initial capacity after 15+ cycles). X-ray diffraction and scanning electron microscopy analysis reveal that thermally stable Al-Ca mixed phases ($\text{Ca}_{12}\text{Al}_{14}\text{O}_{33}$) mitigate crystallite agglomeration and maintain macroporous structures imparted by electrospinning. Nanofibers and Al-doped nanofibers (Al:Ca = 2:10) exhibit more than a factor of three longer CO_2 breakthrough time compared to CaO from marble (1650, 6400, and 7500 $\text{mL g}_{\text{sorbent}}^{-1}$ for CaO-marble, 2Al-10Ca-O-nanofibers, and CaO-nanofibers respectively) under reforming conditions, with Al-doped CaO-nanofibers retaining 94% of their initial performance after ten reforming-regeneration cycles, indicating their potential as improved sorbents for SE-SMR processes.

attractive options to mitigate CO_2 emissions. These processes have the additional advantages (compared to traditional CCS) of improved thermodynamics that often lead to a lower energy consumption in addition to carbon emission mitigation.^[5] One prominent example of simultaneous CO_2 capture with chemical reaction is the use of the gas–solid reaction between CO_2 and calcium oxide (CaO) for hydrogen production^[6] via sorption-enhanced steam methane reforming (SE-SMR).^[5,7,8] In SE-SMR, the combination of CO_2 sorption with methane-reforming reactions shifts the reaction equilibrium toward H_2 production, ultimately leading to greater than 90% conversion, with H_2 selectivity greater than 85%.^[9] The combination of reaction and adsorption steps in a single reactor reduces the complexity of the reforming plant by eliminating the need for water–gas shift reactors and pressure swing adsorption downstream of the reforming reactor.^[5] Furthermore, SE-SMR has the potential to operate at much lower temperatures and pressures (723–873 K and 101–304 kPa) than the conventional meth-


ane reforming (1123–1173 K and 1520–2533 kPa) while still achieving the same methane conversion over the same reforming catalyst (Figure S1, Supporting Information). This simpler reactor configuration has the potential to significantly reduce heat and power requirements of reforming (i.e., lower compression costs and lower consumption of natural gas to heat the reactor) while also sequestering the CO_2 byproduct, leading to a “green reforming” process.

CaO-based materials are the predominant sorbents used in SE-SMR because of their high adsorption capacity ($0.79 \text{ g}_{\text{CO}_2} \text{ g}_{\text{CaO}}^{-1}$), adequate reversibility ($\text{CaO} + \text{CO}_2 \leftrightarrow \text{CaCO}_3$; $K_{\text{eq}} = 87$ at 923 K), fast carbonation–calcination kinetics ($E_{\text{carbonation}} = 20 \text{ kJ mol}^{-1}$; $E_{\text{calcination}} = 104 \text{ kJ mol}^{-1}$),^[10] and low material cost.^[11–13] Unfortunately, CaO sorbents (usually derived from natural CaO compounds such as limestone and dolomite) suffer from low conversions (54% after 60 min of reaction of limestone with 10% CO_2 at 923 K)^[14] due to the formation of CaCO_3 product layers that cover CaO surfaces and fill material pores, thereby inhibiting the diffusion of CO_2 to reaction interfaces.^[15] In addition,

1. Introduction

The increased reliance on fossil fuels to meet energy needs has led to increased CO_2 emissions into the atmosphere.^[1,2] Mitigating the impact of CO_2 on the environment by reducing emissions from various industrial processes and large combustion sources is a vital scientific goal.^[3,4] Although much research has been done on postprocess carbon capture and sequestration (CCS), sorption-enhanced processes that trap carbon at the point of generation (i.e., as it is formed in chemical reactions) are also

F. H. Alshafei, L. T. Minardi, D. Rosales, G. Chen, Prof. D. A. Simonetti
Chemical and Biomolecular Engineering Department
University of California-Los Angeles
Los Angeles, CA 90095, USA
E-mail: dasimonetti@ucla.edu

 The ORCID identification number(s) for the author(s) of this article can be found under <https://doi.org/10.1002/ente.201800807>.

DOI: 10.1002/ente.201800807

CaO-based sorbent capacities significantly decrease over multiple cycles (60% loss in initial capacity for limestone after 10 cycles)^[16] due to the sintering of crystallites or agglomeration of the CaO particles.^[17] Indeed, highly active, efficient, and inexpensive adsorbents are critical for the widespread implementation of SE-SMR technology.^[18]

Current research efforts to improve the utilization and durability of CaO-based sorbents include i) the synthesis of calcium-based sorbents from organic and inorganic precursors (instead of naturally derived CaO sources);^[19] ii) doping CaO with various metals;^[20,21] and iii) post-treating the sorbents in an attempt to increase their lifespan.^[22] Studies by Martavaltzi et al.^[23,24] on mixtures of mayenite, $\text{Ca}_{12}\text{Al}_{14}\text{O}_{33}$, and CaO show that aluminum is an attractive additive to improve the stability of calcium oxides, albeit at the expense of the sorption capacity. Furthermore, studies by Di Giuliano et al. and Aloisi et al. have used mayenite CaO mixtures as a stable support for bifunctional nickel catalysts.^[25–27] The objective of this work is to develop CaO-based sorbents that achieve stoichiometric capacity over multiple regeneration cycles by synthesizing materials with controlled crystallite sizes, large intraparticle void volumes, optimal pore structures and chemical compositions, and varied morphologies. Thermal decomposition, hydrothermal dissolution–recrystallization, and electrospinning were used to control the morphological properties of the sorbents. To elucidate the structure–activity relationship of the CaO sorbents, physicochemical properties were determined using X-ray diffraction (XRD), N_2 -physiosorption measurements, scanning electron microscopy (SEM), energy dispersive X-ray spectroscopy (EDS), and transmission electron microscopy (TEM). These characterization data were combined with reaction kinetics experiments via thermogravimetric analysis (TGA) and steam methane reforming to demonstrate that increases in the surface area and porosity and decreases in the particle agglomerate size and crystallite size lead to increases in the effective diffusivities and surface reaction rate constants, which, in turn, leads to an improved capacity. This work demonstrates that i) stoichiometric CO_2 capacity can be achieved using interconnected, highly porous networks of CaO-based nanofibers that consist of small CaO crystallites; and ii) the initial high capacity of electrospun CaO-based materials can be maintained over multiple cycles of reaction and regeneration by rationally incorporating Al into the CaO structure to form $\text{Ca}_{12}\text{Al}_{14}\text{O}_{33}$ phases, which act as a spacer, thus effectively separating the sorbent particles to prevent them from sintering or aggregating, which in turn prevents the porous fibrous structure from collapsing. This work also demonstrates that Al-doped CaO fibers can increase the reaction times in steam methane reforming reactors by more than a factor of three (compared to commercially produced CaO) or can allow these reactors to operate at higher space velocities (i.e., smaller reactor vessels or higher flow rates).

2. Results and Discussion

2.1. Summary of Abbreviations of CaO-Based Materials

Several CaO-based materials were synthesized using various methods and calcium precursors as detailed in the Experimental

Table 1. Summary of naming conventions to identify the differences in synthesis method and calcium precursor for CaO materials studied herein.

Name	Description
CaO-nanofibers	Undoped CaO nanofibers produced via electrospinning
1Al-20Ca-O-nanofibers	Al-doped CaO nanofibers with Al:Ca of 1:20 produced via electrospinning
1Al-10Ca-O-nanofibers	Al-doped CaO nanofibers with Al:Ca of 1:10 produced via electrospinning
3Al-10Ca-O-nanofibers	Al-doped CaO nanofibers with Al:Ca of 3:10 produced via electrospinning
CaO-marble	Commercially sourced marble
CaO-D-nitrate	CaO from thermal decomposition of $\text{Ca}(\text{NO}_3)_2$
CaO-D-acetate	CaO from thermal decomposition of calcium acetate
CaO-H-nitrate	CaO from hydrothermal synthesis using P123 and $\text{Ca}(\text{NO}_3)_2$

Section. **Table 1** lists the abbreviations used to identify these materials throughout the text with a brief description of the material.

2.2. Physicochemical Properties of CaO and Al-Ca-O Sorbents

Ca-based nanofibers were synthesized via electrospinning using polyvinylpyrrolidone (PVP) as the polymer component and $\text{Ca}(\text{NO}_3)_2$ as the calcium precursor. These materials were then thermally treated in air to remove PVP and convert $\text{Ca}(\text{NO}_3)_2$ to CaO (see Experimental Section). TGA experiments were conducted on the PVP- $\text{Ca}(\text{NO}_3)_2$ nanofibers to quantify the extent of PVP removal during the thermal treatment and provide evidence of the conversion to CaO. Figure S2, Supporting Information, shows the TGA curves of pure PVP and PVP- $\text{Ca}(\text{NO}_3)_2$ nanofibers. Pure PVP nanofibers were decomposed under argon at a heating rate of 10 K min^{-1} , whereas PVP- $\text{Ca}(\text{NO}_3)_2$ nanofibers were decomposed under air at a heating rate of 5 K min^{-1} . The heating rate was reduced in the case of PVP- $\text{Ca}(\text{NO}_3)_2$ to mimic the post-thermal treatment conditions described in the Experimental Section. The nanofibers synthesized using pure PVP (MW = 1 300 000) decomposed under argon in two steps, with a total weight loss of $\approx 95\%$. The first-step weight loss of 16% occurred between ambient temperature and 622 K. This weight loss step can be attributed to the evaporation of volatile solvents. The second-step weight loss of 79% from 623 to 763 K can be attributed to the thermal degradation of the polymer chains. It is clear from the TGA curve that the majority of the PVP matrix is removed at temperatures higher than 923 K. Additionally, PVP- $\text{Ca}(\text{NO}_3)_2$ nanofibers decompose under air in multiple steps, with a total weight loss of $\approx 80\%$ (Figure S2, Supporting Information). The first step weight loss of 12% occurred between ambient temperature and 360 K and can be attributed to the evaporation of volatile solvents. The second weight loss of 27% from 580 to 620 K can be attributed to the combustion of PVP in the presence of oxygen. The third gradual weight loss of 14% from 620 to 770 K can be attributed to the oxidation of residual carbon remaining on the nanofibers. The final weight loss of 24% from 770 to 790 K can be attributed

to the decomposition of calcium nitrate $[\text{Ca}(\text{NO}_3)_2]$ to CaO, indicating that the thermal treatments of PVP- $\text{Ca}(\text{NO}_3)_2$ nanofibers result in the formation of CaO nanofibers without residual carbon.

XRD was used to identify the crystalline phases and average crystal sizes of the CaO and Al-Ca-O sorbents prepared using the synthesis techniques described in the Experimental Section. **Figure 1a** (black) shows the XRD patterns of the as-synthesized, undoped PVP- $\text{Ca}(\text{NO}_3)_2$ nanofibers before thermal treatment at 923 K. Well-defined diffraction peaks are absent from the XRD pattern, which indicates that the nanofibers consist of amorphous polymer phases and calcium species that are too small to diffract X-rays. **Figure 1a** also shows the XRD patterns of CaO-nanofibers (red), CaO-D-acetate (purple), CaO-D-nitrate (green), and CaO-H-nitrate (blue), after undergoing thermal treatment. **Figure S4**, Supporting Information, shows the XRD patterns for CaO-marble and CaO-marble after the reaction-regeneration cycle. Crystalline peaks of both CaO (■) and $\text{Ca}(\text{OH})_2$ (●) were identified. $\text{Ca}(\text{OH})_2$ was formed after the samples adsorbed moisture from the atmosphere because of

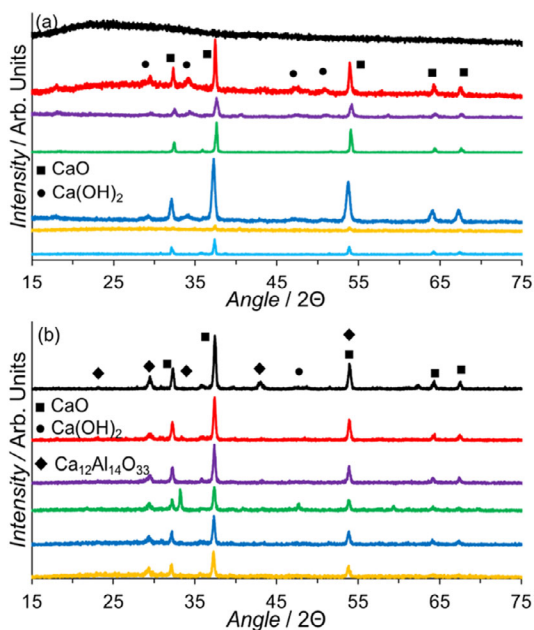


Figure 1. a) XRD patterns of (black) PVP- $\text{Ca}(\text{NO}_3)_2$ nanofibers prepared via electrospinning prior to thermal treatment: CaO-nanofibers after thermal treatment in air (923 K, 101 kPa) (red); CaO-D-acetate (produced via thermal decomposition of calcium acetate in air at 1023 K, 101 kPa) (purple); CaO-D-nitrate (produced via thermal decomposition of calcium nitrate in air at 923 K, 101 kPa) (green); CaO-H-nitrate (produced hydrothermally using calcium nitrate and P123 surfactant) (blue); CaO-nanofibers after ten cycles (orange); and CaO-D-nitrate after ten cycles (light blue). b) XRD patterns of Al-doped electrospun CaO materials: 3Al-10Ca-O-nanofibers (black); 1Al-10Ca-O-nanofibers (red); 1Al-20Ca-O-nanofibers (purple); 3Al-10Ca-O-nanofibers after 17 cycles (green); 1Al-10Ca-O-nanofibers after 16 cycles (blue); and 1Al-20Ca-O-nanofibers after 16 cycles (orange). Characteristic peaks for CaO, $\text{Ca}(\text{OH})_2$, $\text{Ca}_{12}\text{Al}_{14}\text{O}_{33}$ are indicated by squares, circles, and diamonds, respectively. One cycle consists of reaction (in a TGA) with ambient pressure of pure CO_2 at 823 K followed by reaction with air at ambient pressure and 1073 K (see Experimental Section for complete details).

the hygroscopic nature of CaO.^[28] The edge length of the unit cell of the five CaO sorbents was calculated from the peak at $2\theta = 37^\circ$ in XRD patterns. Each sample had a lattice parameter of 4.8 Å, confirming that the samples consist of cubic CaO. Average crystallite sizes were calculated from the peak at $2\theta = 37^\circ$ using Scherrer's equation (**Table 2**). The average crystal domain sizes of CaO-nanofibers, CaO-D-acetate, CaO-D-nitrate, CaO-H-nitrate, and CaO-marble were 39 nm, 33 nm, 64 nm, 35 nm, and 84 nm, respectively, confirming that CaO derived from natural sources (in this case, marble) has significantly larger crystallite sizes than CaO derived from organometallic sources. The XRD patterns of the CaO sorbents that have undergone multiple cycles of reaction with CO_2 followed by reaction with air (i.e., reaction-regeneration cycles) are shown in **Figure 1a** (yellow and light blue) and **Figure S4**, Supporting Information, (red) and are discussed in subsequent sections.

Figure 1b shows the XRD patterns of the three Al-doped CaO-based nanofibers after undergoing thermal treatment at 1173 K (see Experimental Section). Crystalline peaks corresponding to mayenite^[29] ($\text{Ca}_{12}\text{Al}_{14}\text{O}_{33}$) are evident in the XRD data as well as peaks corresponding to CaO. The XRD data confirm that $\text{Ca}_{12}\text{Al}_{14}\text{O}_{33}$, a stable composite metal, was integrated successfully into the CaO sorbent to serve as a binder or a spacer (as discussed subsequently). The average crystal domain sizes of the Al-doped electrospun materials were 53 nm (3Al-10Ca-O-nanofibers), 50 nm (1Al-10Ca-O-nanofibers), and 50 nm (1Al-20Ca-O-nanofibers). **Figure 1b** also shows the XRD patterns of the Al-doped CaO-nanofibers after multiple reaction-regeneration cycles, and these results are discussed in subsequent sections.

N_2 -physorption was used to determine the surface area, pore volume, and average pore diameter of the CaO samples (**Table 2**). The CaO-nanofibers ($16 \text{ m}^2 \text{ g}^{-1}$), CaO-D-acetate ($17 \text{ m}^2 \text{ g}^{-1}$), and CaO-H-nitrate ($16 \text{ m}^2 \text{ g}^{-1}$) samples exhibited more than twice the surface area of CaO-marble ($7.6 \text{ m}^2 \text{ g}^{-1}$) and more than three times the surface area of CaO-D-nitrate ($4.8 \text{ m}^2 \text{ g}^{-1}$). Similarly, the BJH pore volumes of the CaO-nanofibers ($0.092 \text{ cm}^3 \text{ g}^{-1}$), CaO-D-acetate ($0.110 \text{ cm}^3 \text{ g}^{-1}$), and CaO-H-nitrate ($0.099 \text{ cm}^3 \text{ g}^{-1}$) samples were a factor of three higher than the CaO-marble sample ($0.034 \text{ cm}^3 \text{ g}^{-1}$) and a factor of 30 higher than the CaO-D-nitrate sample ($0.0032 \text{ cm}^3 \text{ g}^{-1}$). The chemically synthesized samples, with the exception of CaO-D-nitrate (2.7 nm), also had larger BJH average pore diameters (CaO-nanofibers: 13.1 nm, CaO-D-acetate: 13.9 nm, CaO-H-nitrate: 18.6 nm) compared with CaO-marble (9.5 nm). These data indicate that the techniques used to synthesize CaO from organometallic precursors (i.e., hydrothermal treatment and electrospinning) lead to highly porous materials that retain their pore structure even after thermal treatments to convert the calcium precursors to CaO.

SEM was used to probe the effect of synthesis technique and calcium source on sorbent morphology at the micrometer scale. **Figure 2a,b** shows the SEM image (5000 and 20 000 times magnification) of the as-synthesized PVP- $\text{Ca}(\text{NO}_3)_2$ nanofibers before thermal treatment. The electrospun fibers consisted of uniform, continuous, and smooth nanofibers with circular cross sections. The fibers had a narrow distribution with a mean diameter of $180 \pm 57 \text{ nm}$ (see **Figure S3**, Supporting Information) and lengths of up to several hundred micrometers. As seen

Table 2. Properties of CaO and Al-Ca-O sorbents.

Sorbent	S_{BET} [$\text{m}^2 \text{g}^{-1}$] ^{a)}	V_{pore} [$\text{cm}^3 \text{g}^{-1}$] ^{b)}	Pore diameter [nm] ^{b)}	Crystallite size [nm] ^{c)}	Postcycled crystallite size [nm] ^{c)}	Al/Ca ^{d)}
CaO-marble	7.6	0.034	9.5	84	76 [10 cycles]	–
CaO-D-acetate	17	0.110	13.9	33	62 [10 cycles]	–
CaO-D-nitrate	4.8	0.003	2.7	64	73 [10 cycles]	–
CaO-H-nitrate	16	0.010	18.6	35	–	–
CaO-nanofibers	16	0.092	13.1	39	64 [10 cycles]	–
3Al-10Ca-O-nanofibers	–	–	–	53	50 [17 cycles]	0.29
1Al-10Ca-O-nanofibers	–	–	–	50	46 [16 cycles]	0.10
1Al-20Ca-O-nanofibers	–	–	–	50	48 [16 cycles]	0.045

^{a)}Calculated by BET method; ^{b)}Calculated by BJH method; ^{c)}Based on XRD; ^{d)}Obtained by EDS.

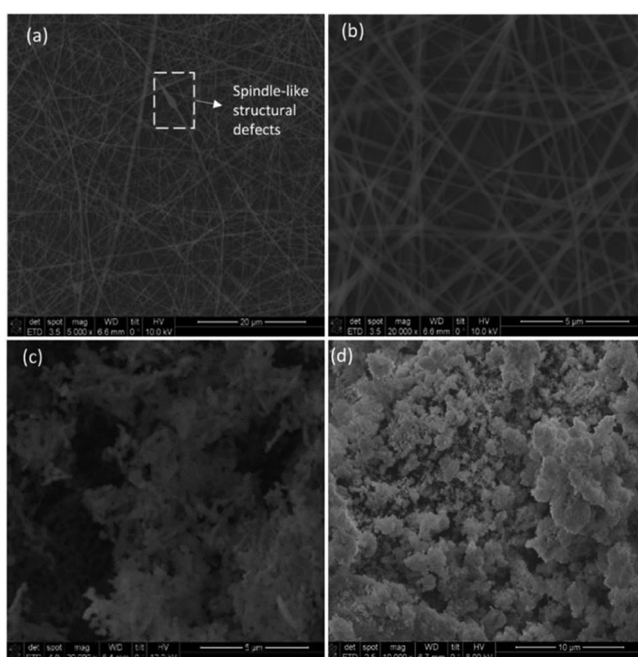


Figure 2. SEM images of as-synthesized PVP-Ca(NO₃)₂ nanofibers at a) 5000× (14 mm = 20 μm) and b) 20 000× magnification (14 mm = 5 μm). c) CaO-nanofibers synthesized via electrospinning and thermally treated in air at 923 K (14 mm = 5 μm). d) CaO-nanofibers after 10 cycles (14 mm = 10 μm).

from Figure 2a, a few spindle-like structural defects with an average diameter of 1.3 μm were present, and these defects were possibly formed from transient instabilities experienced by the travelling jet during the electrospinning process.^[30,31] On thermal treatment at 923 K, CaO-nanofibers were obtained as indicated by the XRD analysis (discussed previously). The post-thermally treated fibers (CaO-nanofibers) had a mean diameter of 208 ± 53 nm (Figure S3b, Supporting Information). By comparing the SEM images of the nanofibers before (Figure 2a,b) and after thermal treatment (Figure 2c), it becomes clear that the thermal treatment transforms the PVP-Ca(NO₃)₂ fibers from smooth and continuous nanofibers, which are cylindrical in shape, to a network of nanoparticles that are closely

connected in a nanofibrous structure with considerable macroporous (>300 nm diameter) intraparticle void volume. This change in morphology occurs, of course, because of the degradation of the polymer chains and the formation of CaO at these elevated temperatures.

Figure S5a–e, Supporting Information, shows the SEM images of the remaining nondoped CaO sorbents (CaO-marble, CaO-D-acetate, CaO-D-nitrate, and CaO-H-nitrate) after undergoing thermal treatment and shows CaO-marble after a reaction–regeneration cycle. Both CaO-marble and CaO-D-nitrate had considerably large average agglomerate sizes, with the marble-derived sorbent having sizes of $\approx 835 \pm 262$ nm (measured from the SEM micrograph using ImageJ) and CaO-D-nitrate having agglomerates in the micrometer range. The agglomerate sizes of these two sorbents were a factor four or more larger than the other sorbents, with CaO-nanofibers having the smallest average agglomerate size of 184 ± 33 nm of the nondoped sorbents. Smaller agglomerate/particle sizes, in general, are believed to contribute to enhanced sorption performance due to their larger surface-to-volume ratios.^[32] The SEM images in Figure S5a–d, Supporting Information, also reveal that CaO samples prepared from the decomposition of calcium acetate and nitrate and from the hydrothermal treatment of CaO (using calcium nitrate as a precursor) have uneven surface textures with considerably rough and sharp edges. On the other hand, the marble-derived CaO and electrospun CaO nanofibers have well-defined, rounder, and smoother structures, with the nanofibers having a noticeably smaller domain size and visibly larger macro-sized void volumes.

Figure 3a–c shows the SEM images of the Al-doped CaO sorbents (3Al-10Ca-O-nanofibers, 1Al-10Ca-O-nanofibers, and 1Al-20Ca-O-nanofibers). The SEM images reveal that all the Al-containing nanofibers have morphologically similar features as the nondoped CaO-nanofibers sorbent (Figure 2), albeit with slightly smaller domain sizes. The reduction in the domain size of the Al-Ca-O sorbents is believed to be due to the higher metal content present in the electrospinning solution (i.e., more aluminum nitrate ions), which increases the conductivity of the electrospinning solution, which in turn yields thinner fibers.^[33,34] In addition to SEM, EDS analysis was performed on the Al-doped samples to confirm the atomic ratio of Al to Ca in the formed sorbents. Table 2 shows the Al/Ca ratios obtained from the SEM/EDS analysis.

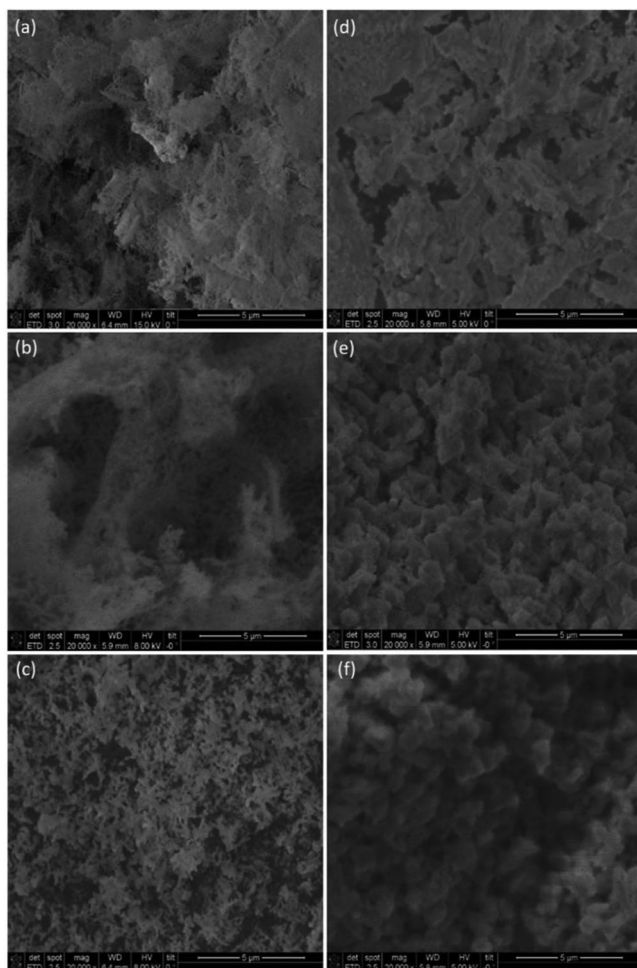


Figure 3. SEM images (15 mm = 20 μm) of a) 3Al-10Ca-O-nanofibers, b) 1Al-10Ca-O-nanofibers, c) 1Al-20Ca-O-nanofibers, d) 3Al-10Ca-O-nanofibers after 17 cycles, e) 1Al-10Ca-O-nanofibers after 16 cycles, and f) 1Al-20Ca-O-nanofibers after 16 cycles.

Figure 2d, 3d–f shows the SEM images of the CaO nanofibers (pure and Al-doped) following 10–17 cycles of carbonation and calcination. As seen from the SEM images, the nondoped CaO sorbents (CaO-marble in Figure S5e, Supporting Information, and CaO-nanofibers in Figure 2d) suffered from severe morphological changes after 10 cycles, whereas the Al-doped samples (Figure 3d–f) were able to retain several morphological features (particularly, their macro-sized void volumes and fibrous structure) even after 16–17 cycles. The degree of resistance to sintering and change in morphology was, indeed, more pronounced in the samples that contained Al, especially those with higher Al to Ca ratios, as evidenced by the SEM images (Figure 3d–f). The significance of these results and its impact on performance and sorbent stability are discussed in more depth in the subsequent sections.

TEM analysis (Figure 4) was performed on four nondoped CaO sorbents (CaO-marble, CaO-D-acetate, CaO-H-nitrate, and CaO-nanofibers) to supplement the SEM analysis and determine the impact of synthesis approach on morphology. TEM images (Figure 4a) reveal that CaO derived from marble consists of large,

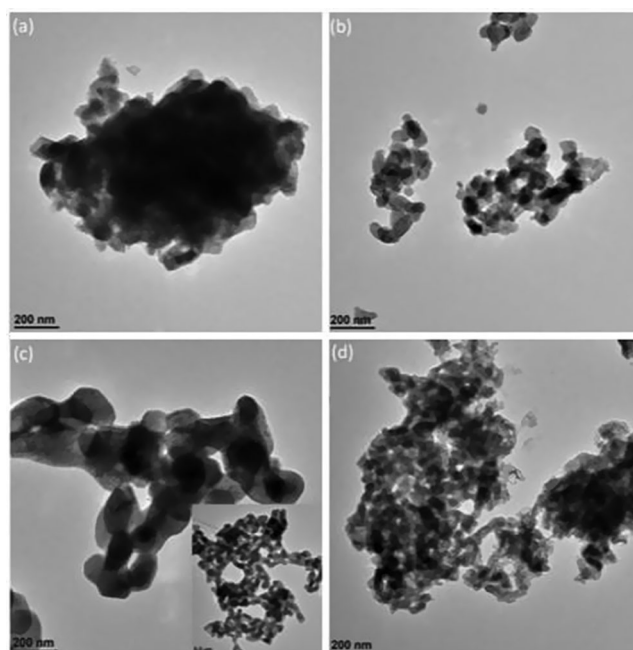


Figure 4. TEM images of a) CaO derived from marble (CaO-marble), b) CaO synthesized from the thermal decomposition of calcium nitrate at 1023 K followed by treatment with an aqueous solution of P123 (CaO-H-nitrate), c) CaO-nanofibers synthesized via electrospinning and thermally treated in air at 923 K (CaO-nanofibers), and d) CaO synthesized from thermal decomposition of calcium acetate in air 1023 K (CaO-D-acetate). The inset image in panel (c) shows a wider view image of CaO-nanofibers (4 mm = 0.5 μm) with the red arrow pointing to the region shown in the main image.

closely packed and multilayered nanoparticles, with sizes ranging from roughly 50 to 180 nm. The CaO-H-nitrate (Figure 4b) and CaO-D-acetate samples (Figure 4d) had comparatively smaller nanoparticles (≈25–120 nm) than CaO-marble. The electrospun CaO-nanofibers (Figure 4c) had nanoparticles with diameters ranging from ≈70–180 nm; however, they contained significantly larger macroporous intraparticle void volumes. These intraparticle spaces appear as void channels (inset of Figure 4c) and have diameters that are on the order of 0.5 μm.

2.3. Initial Carbonation Capacity and Kinetics

TGA experiments were conducted on the five nondoped CaO samples (CaO-marble, CaO-D-acetate, CaO-D-nitrate, CaO-H-nitrate, and CaO-nanofibers) to compare their CO₂ sorption capacity and reaction rates. Figure 5 shows the first-cycle carbonation reaction curves (in terms of conversion of CaO to CaCO₃ and capacity [g_{CO₂}/g_{CaO}] vs time on stream) at three temperatures (823, 873, and 923 K). From the experimental carbonation curves, the conversion seems to evolve with time in two stages: a fast chemical reaction-controlled stage followed by a slower increase that is controlled by the diffusion of molecules (and possibly atoms) through solid product layers.^[35] TGA experiments were stopped after 60 min because at this time the conversion seems to approach a constant value with increasing time on stream.

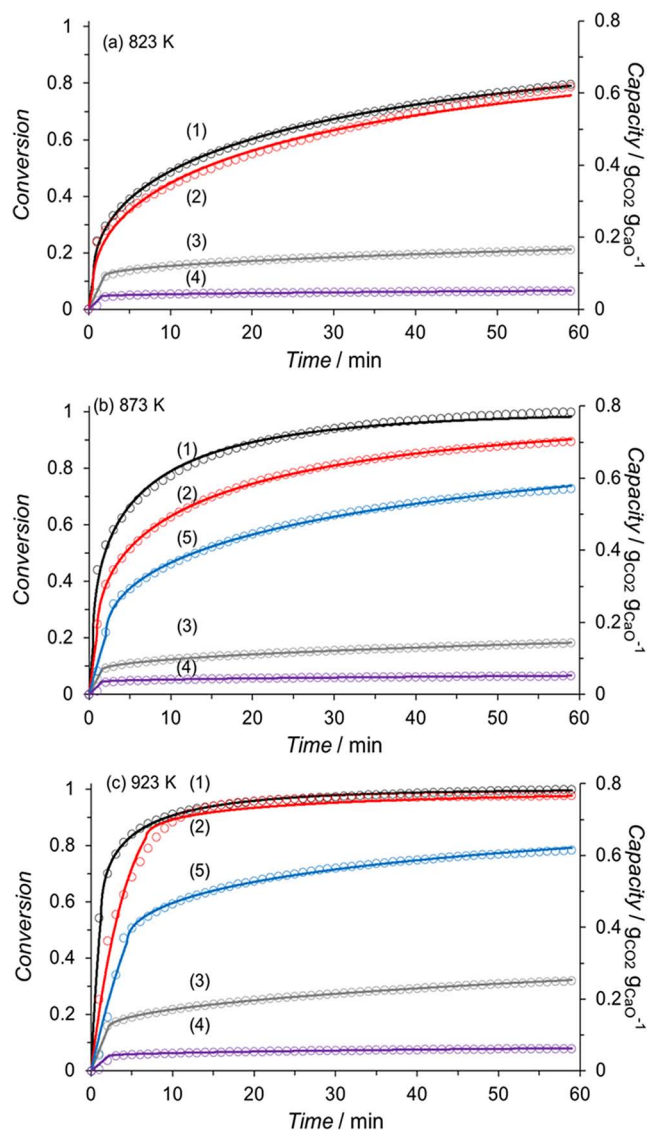


Figure 5. Experimental conversion, sorption capacities, and RPM prediction of conversion (dashed lines) for 1) CaO-nanofibers, 2) CaO-D-acetate, 3) CaO-marble, 4) CaO-D-nitrate, and 5) CaO-H-nitrate measured by TGA at a) 823 K, b) 873 K, and c) 923 K, 101 kPa, and with 200 sccm of CO₂.

The differences in conversion among the five samples (reported in Table S1, Supporting Information) indicate the effect of morphological features and physicochemical properties on CO₂ sorption. CaO-marble, a sample that has large agglomerate, particle, and crystallite sizes as well as a low surface area and intraparticle void volume (as discussed previously), exhibited conversions of 20% (0.17 g_{CO₂} g_{CaO}⁻¹) at 823 K, 18% (0.14 g_{CO₂} g_{CaO}⁻¹) at 873 K, and 32% (0.25 g_{CO₂} g_{CaO}⁻¹) at 923 K, in agreement with previous studies.^[14,36] Additionally, CaO-D-nitrate, another sample with a relatively large crystallite size and small surface area and pore volume (an order of magnitude smaller than CaO-marble as shown in Table 2), exhibited conversions of 6.5% (0.05 g_{CO₂} g_{CaO}⁻¹) at 823 K, 6.5% (0.05 g_{CO₂} g_{CaO}⁻¹) at 873 K, and 8% (0.06 g_{CO₂} g_{CaO}⁻¹)

at 923 K. The decrease in reactive surface area and pore volume for CO₂ diffusion resulted in approximately a fourfold decrease in conversion. On the other hand, the CaO samples synthesized from the decomposition of calcium acetate (CaO-D-acetate) and hydrothermal treatment of CaO (CaO-H-nitrate) exhibited more than threefold higher conversions than CaO-marble and CaO-D-nitrate at all temperatures (Table S1), with CaO-nanofibers achieving stoichiometric CO₂ capacity (0.79 g_{CO₂} g_{CaO}⁻¹) in less than 1 h of reaction at both 873 and 923 K. The higher conversion of the CaO-D-acetate, CaO-H-nitrate, and CaO-nanofibers provides evidence to support the conclusion that structures with small crystallites and high porosity (high surface area and intraparticle void volume) enhance the reactivity of CaO materials and reduce their susceptibility to transport limitations from the formation of product layers that cover surfaces and fill pores.

The CaO-nanofiber sample also exhibited higher capacity (0.79 g_{CO₂} g_{CaO}⁻¹ at 873 and 923 K) compared with CaO-D-acetate (0.70 and 0.77 g_{CO₂} g_{CaO}⁻¹ at 873 and 923 K, respectively) and CaO-H-nitrate (0.59 and 0.62 g_{CO₂} g_{CaO}⁻¹ at 873 and 923 K, respectively). These three samples all consisted of similar particle and crystallite sizes, surface areas, and mesopore volumes (Table 2); therefore, the higher capacity of the nanofibers could potentially be attributed in part to the larger intramacroporosity (i.e., particle void spaces and intraparticle channels) within the nanofiber networks imparted by the electrospinning synthesis technique as shown via TEM in Figure 4c. Furthermore, the CaO-H-nitrate sample synthesized by hydrothermal treatment in our studies exhibited a much higher conversion (73% at 873 K) compared with the thermally decomposed Ca(NO₃)₂ (CaO-D-nitrate) (6.5% at 873 K). The low conversion of CaO synthesized from the simple thermal decomposition of Ca(NO₃)₂ (CaO-D-nitrate) is consistent with the values reported by Lu et al.^[19] (2.5%) for such materials. Therefore, the studies reported herein indicate that the synthesis technique plays a pivotal role in dictating the sorbent capacity of a CaO-based material by controlling the morphology and properties such as crystallite size, surface area, pore volume, pore diameter, and intraparticle void volumes. Hydrothermal treatment and electrospinning were found to alter the macroporosity of the sample (pores on the order of 0.5 μm as identified in SEM and TEM images); introduction of these macropores possibly abates diffusional restrictions from pore filling and surface coverage effects, thus leading to higher sorption capacities.

To quantify the observed differences in performance described in the previous paragraphs, the results from the TGA experiments were analyzed using the random pore model (RPM; see Experimental Section). The RPM models the rate of change of pore radii at the initial stages of conversion using a reaction rate equation that is first order in the concentration of CO₂ and normalized by the surface area of the material. Thus, the reaction rate constant (k_{RPM}) in this equation is also normalized by surface area and reflects the rate of chemical reaction at the surface. Nonreactive CaCO₃ surfaces serve as diffusional barriers, and as these nonreactive product surfaces grow and intersect with each other, the system transitions into a diffusion-controlled regime. The effective diffusivity (D_{RPM}) quantitatively characterizes this regime and reflects the differences in the product layer thickness and penetrability.

Values for k_{RPM} and D_{RPM} (Table 3) were determined using Athena Visual Studio. RPM model predictions (lines) are shown in Figure 5 (overlaid with experimental conversion data points). The rate constants exhibit an exponential dependence on inverse temperature (Figure 6), and the activation energies for the reaction ($E_a = 9, 20, 31,$ and 73 kJ mol^{-1} for CaO-D-nitrate, CaO-marble, CaO-D-acetate, and CaO-nanofibers, respectively) are within similar ranges as in the previous studies ($E_a = 28.4 \text{ kJ mol}^{-1}$ as reported by Zhou et al.^[37]). Values for k_{RPM} for CaO-H-nitrate ($2.5 \times 10^{-4} \pm 1.2 \times 10^{-6}$ and $3.1 \times 10^{-4} \pm 1.7 \times 10^{-6} \text{ cm}^4 \text{ mol}^{-1} \text{ s}^{-1}$ at 873 and 923 K, respectively) are similar to those for CaO-D-nitrate ($2.1 \times 10^{-4} \pm 1.1 \times 10^{-6}$ and $2.3 \times 10^{-4} \pm 1.3 \times 10^{-5} \text{ cm}^4 \text{ mol}^{-1} \text{ s}^{-1}$ at 873 and 923 K, respectively) and CaO-marble ($3.1 \times 10^{-4} \pm 1.2 \times 10^{-6}$ and $3.8 \times 10^{-4} \pm 2.0 \times 10^{-6} \text{ cm}^4 \text{ mol}^{-1} \text{ s}^{-1}$ at 873 and 923 K, respectively), as expected for materials that are chemically similar (i.e., crystalline CaO). However, the D_{RPM} values for CaO-H-nitrate ($4.7 \times 10^{-12} \pm 1.9 \times 10^{-14}$ and $3.6 \times 10^{-12} \pm 5.1 \times 10^{-14} \text{ cm}^2 \text{ s}^{-1}$ at 873 and 923 K, respectively) are 5–10 times larger than CaO-marble ($2.0 \times 10^{-13} \pm 1.0 \times 10^{-15}$ and $9.0 \times 10^{-13} \pm 5.0 \times 10^{-15} \text{ cm}^2 \text{ s}^{-1}$ at 873 and 923 K, respectively). Additionally, the D_{RPM} values for CaO-D-nitrate ($2.0 \times 10^{-14} \pm 1.0 \times 10^{-15}$ and $4.0 \times 10^{-14} \pm 6.0 \times 10^{-15} \text{ cm}^2 \text{ s}^{-1}$ at 873 and 923 K, respectively) are approximately an order of magnitude smaller than those for CaO-marble. Thus, we conclude that the modification of CaO via hydrothermal treatment in the presence of P123 leads to CaO domains with similar reactivity as CaO-D-nitrate and CaO-marble, but the CaO-H-nitrate sample exhibits better conversion during carbonation because of smaller domain sizes (crystallites and particles) and higher porosity.

In contrast to CaO-H-nitrate, the higher k_{RPM} values (Table 3) for CaO-D-acetate ($3.2 \times 10^{-4} \pm 1.4 \times 10^{-5}, 5.0 \times 10^{-4} \pm 2.5 \times 10^{-6},$ and $5.2 \times 10^{-4} \pm 4.8 \times 10^{-6} \text{ cm}^4 \text{ mol}^{-1} \text{ s}^{-1}$ at 823, 873, and 923 K, respectively) and CaO-nanofibers ($4.6 \times 10^{-4} \pm 4.2 \times 10^{-6}, 8.9 \times 10^{-4} \pm 1.8 \times 10^{-5},$ and $1.5 \times 10^{-3} \pm 9.5 \times 10^{-6} \text{ m}^4 \text{ mol}^{-1} \text{ s}^{-1}$ at 823, 873, and 923 K, respectively) compared with CaO-marble indicate a difference in the surface chemistry of the reaction despite their chemical similarity (i.e., crystalline CaO), beyond the effects of superior pore structure that ameliorates diffusion restrictions. This enhanced reactivity with decreasing particle size, similar to that observed in catalysis by metal particles,^[38,39] may result from the preferential exposure of high index planes that comprise smaller crystallites^[40] or from CaO structures that are inherently imparted by the synthesis technique with lesser extents of long range order. Values of D_{RPM} are also larger

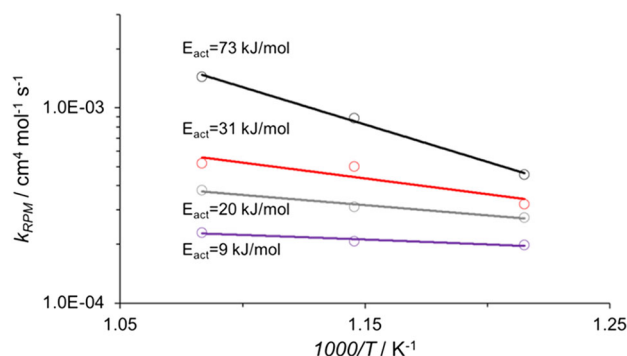


Figure 6. Arrhenius plots for reaction of CaO-nanofibers (black), CaO-D-acetate (red), CaO-marble (gray), and CaO-D-nitrate (purple). Circles represent experimentally determined reaction rate parameters for the random pore model determined from regression of conversion versus time data in Figure 5. Activation energies were determined by least squares regression of the experimentally determined parameters (lines).

for CaO-D-acetate ($4.2 \times 10^{-12} \pm 5.6 \times 10^{-14}, 1.4 \times 10^{-11} \pm 3.7 \times 10^{-14},$ and $7.8 \times 10^{-12} \pm 2.1 \times 10^{-13} \text{ cm}^2 \text{ s}^{-1}$ at 823, 873, and 923 K, respectively) and CaO-nanofibers ($7.2 \times 10^{-12} \pm 1.9 \times 10^{-14}, 4.3 \times 10^{-11} \pm 3.0 \times 10^{-13},$ and $5.5 \times 10^{-11} \pm 8.2 \times 10^{-13} \text{ cm}^2 \text{ s}^{-1}$ at 823, 873, and 923 K, respectively) compared with CaO-marble (Table 3) indicating the effect of smaller reactive domains and possibly the formation of thinner CaCO_3 layers with structures that are more easily penetrable by gaseous CO_2 .^[41–43]

2.4. Multicycle Reaction–Regeneration of CaO

Ten cycles of carbonation and calcination were performed to study the stability of the CaO sorbents (CaO-marble, CaO-D-nitrate, CaO-D-acetate, and CaO-nanofibers) and the reversibility of the carbonation reaction. CaO-marble lost 1% (0.2 mg) of its initial sorption capacity after the first carbonation–oxidation cycle. Figure 7 shows the sorption capacity of CaO-marble, CaO-D-nitrate, CaO-D-acetate, and CaO-nanofibers over 10 carbonation and calcination cycles. The CaO-marble reached 12% ($0.10 \text{ gCO}_2 \text{ gCaO}^{-1}$) conversion on its 10th carbonation cycle, losing $\approx 34\%$ of its initial capacity. The CaO-D-nitrate reached 4.5% ($0.036 \text{ gCO}_2 \text{ gCaO}^{-1}$) conversion on its 10th carbonation cycle, losing $\approx 30\%$ of its initial capacity. The CaO-D-acetate reached 29% ($0.23 \text{ gCO}_2 \text{ gCaO}^{-1}$) conversion on its 10th carbonation cycle, losing $\approx 66\%$ of its initial capacity. The electrospun CaO sorbent

Table 3. RPM parameters and 95% confidence intervals derived from the carbonation data in Figure 5.

Sample	823 K		873 K		923 K	
	$k_{RPM} [\times 10^4]$ [$\text{cm}^4 \text{ mol}^{-1} \text{ s}^{-1}$]	$D_{RPM} [\times 10^{12}]$ [$\text{cm}^2 \text{ s}^{-1}$]	$k_{RPM} [\times 10^4]$ [$\text{cm}^4 \text{ mol}^{-1} \text{ s}^{-1}$]	$D_{RPM} [\times 10^{12}]$ [$\text{cm}^2 \text{ s}^{-1}$]	$k_{RPM} [\times 10^4]$ [$\text{cm}^4 \text{ mol}^{-1} \text{ s}^{-1}$]	$D_{RPM} [\times 10^{12}]$ [$\text{cm}^2 \text{ s}^{-1}$]
CaO-marble	2.8 ± 0.007	0.2 ± 0.002	3.1 ± 0.012	0.20 ± 0.001	3.8 ± 0.020	0.9 ± 0.005
CaO-D-acetate	3.2 ± 0.135	4.2 ± 0.056	5.0 ± 0.025	13.6 ± 0.037	5.2 ± 0.048	7.8 ± 0.206
CaO-D-nitrate	2.0 ± 0.010	0.02 ± 0.001	2.1 ± 0.011	0.02 ± 0.001	2.3 ± 0.134	0.04 ± 0.006
CaO-H-nitrate	–	–	2.5 ± 0.012	4.70 ± 0.019	3.1 ± 0.017	3.6 ± 0.051
CaO-nanofibers	4.6 ± 0.042	7.2 ± 0.019	8.9 ± 0.177	42.9 ± 0.298	14.5 ± 0.095	55.0 ± 0.822

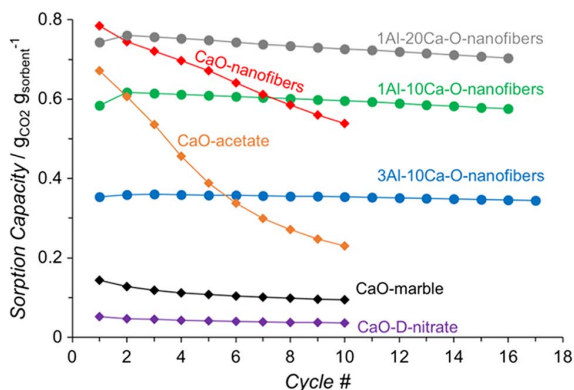


Figure 7. Sorption capacity of CaO-marble (black, diamonds), CaO-D-nitrate (purple, diamonds), CaO-D-acetate (orange, diamonds), CaO-nanofibers (red, diamonds), 3Al-10Ca-O-nanofiber (blue, circles), 1Al-10Ca-O-nanofiber (green, circles), 1Al-20Ca-O-nanofiber (grey, circles) across multiple reaction–regeneration cycles at 873 K, 101 kPa, and 200 sccm of CO₂ via TGA.

reached 69% ($0.54 \text{ g}_{\text{CO}_2} \text{ g}_{\text{CaO}}^{-1}$) conversion on its 10th carbonation cycle, losing 31% of its initial capacity. The CaO-nanofibers sorbent retains a relatively high capacity even after 10 cycles of carbonation–calcination, although its loss of initial capacity is proportionally similar to CaO-marble and CaO-D-nitrate.

CaO samples after reaction–regeneration cycles (CaO-marble, CaO-D-acetate, CaO-D-nitrate, and CaO-nanofibers) were also treated at 923 K for 8 h at 5 K min^{-1} to minimize the impact of hydroxide formation via exposure to ambient air and immediately analyzed using XRD, as seen in Figure S4 (red), S6, Supporting Information, and Figure 1a (yellow and light blue). The crystallite sizes of the sorbents after these cycles (Table 2) were calculated based on the peak at $2\theta = 37^\circ$. The calculated crystallite sizes of CaO-marble, CaO-D-nitrate, CaO-D-acetate, and CaO-nanofibers were 76 nm, 73 nm, 62 nm, and 64 nm, respectively. The crystallite sizes of CaO-marble and CaO-D-nitrate remained relatively unchanged after cycling because the formation of this sample likely occurred at conditions that led to sintering and agglomeration. In contrast, the crystallite sizes of CaO-D-acetate and CaO-nanofibers increased from 33 nm to 62 nm and 39 nm to 64 nm, respectively. The sintering and aggregation of the crystallites in the CaO-D-acetate and CaO-nanofibers are likely the reason for the loss in activity of the sorbent over repeated cycles in addition to possible loss of pore structure and volume.^[10,16,44]

SEM analysis, as discussed previously, was also performed on the cycled CaO-marble and CaO-nanofibers samples to investigate the effect of multiple reaction–regeneration cycles on morphology (Figure S5a,e, Supporting Information, and Figure 2d). The SEM images of the thermally treated CaO-marble (Figure S4e, Supporting Information) and CaO-nanofibers (Figure 2d) reveal that cycling detrimentally affected the morphology of the oxide fibers, especially the CaO-nanofiber sample that underwent drastic structural and morphological changes. Specifically, the SEM image shows that upon cycling, the CaO-nanofibers sample lost its porous, fibrous structure, which was initially responsible for mitigating pore plugging. This loss

of nanoscale structure results in the reduction seen in the sorption capacity of CaO-nanofibers upon multiple cycling. The post-cycle SEM images also reveal that after 10 cycles both samples consisted of agglomerated, irregularly shaped nanoparticles. Therefore, although electrospinning results in the formation of CaO nanostructures that are highly active, repeated calcinations collapse the fibrous structure, and strategies such as metal doping may be required to maintain the morphology and thus the initial high sorption capacity of the active materials prepared via electrospinning.

2.5. Multicycle Reaction–Regeneration of Electrospun Aluminum-Doped CaO

Reaction–regeneration cycles were also collected for the Al-doped CaO nanofibers to study the balance between improved stability and decreased sorption capacity due to the introduction of aluminum. As seen in Figure 7, the initial sorption capacities of 3Al-10Ca-O-nanofibers, 1Al-10Ca-O-nanofibers, and 1Al-20Ca-O-nanofibers at 873 K were 0.35 , 0.58 , and $0.74 \text{ g}_{\text{CO}_2} \text{ g}_{\text{sorbent}}^{-1}$, respectively. By comparing those values to the initial sorption capacity of CaO-nanofibers ($0.79 \text{ g}_{\text{CO}_2} \text{ g}_{\text{sorbent}}^{-1}$ at 873 K), it becomes evident that doping CaO with aluminum decreases the capacity of the sorbent proportional to the quantity of aluminum added. After 16 cycles, the sorption capacities of 3Al-10Ca-O-nanofibers, 1Al-10Ca-O-nanofibers, and 1Al-20Ca-O-nanofibers were 0.35 , 0.58 , and $0.70 \text{ g}_{\text{CO}_2} \text{ g}_{\text{sorbent}}^{-1}$, respectively. As evident from Figure 7, all the Al-doped nanofibers retained >95% of their initial capacity throughout cycling, with the sample containing 3:10 Al:Ca (3Al-10Ca-O-nanofibers) retaining $\approx 98\%$ of its initial capacity, even after 17 cycles.

After completing the cycling tests, all three postcycled samples were thermally treated at 923 K for 8 h at 5 K min^{-1} to minimize the impact of hydroxide formation via exposure to ambient air and immediately analyzed using XRD and SEM. Figure 1b (lines 4–6) shows the XRD patterns of the Al-Ca-O sorbents, and Table 2 shows the crystallite sizes calculated using Scherrer's formula based on the crystallite peak at $2\theta = 37^\circ$. As shown in Table 2, the crystallite sizes of the three Al-doped materials remained unchanged, as the calculated crystallite sizes of 3Al-10Ca-O-nanofibers, 1Al-10Ca-O-nanofibers, and 1Al-20Ca-O-nanofibers were 53, 50, and 50 nm, respectively, before cycling and 50, 46, and 48 nm, respectively, after cycling. As discussed previously, the crystallite size of the un-doped CaO-nanofibers increased from 39 to 64 nm after only 10 cycles under similar reaction conditions. Therefore, we conclude that Al addition forms $\text{Ca}_{12}\text{Al}_{14}\text{O}_{33}$ phases (identified by XRD as described previously) that are dispersed within CaO particles and that stabilize CaO crystallites by abating sintering over the course of reaction–regeneration cycling.

SEM analysis, as discussed previously, was also performed on the postcycled Al-doped sorbents to investigate the cycling effect on morphology. Figure 3d–f shows the SEM images of the postcycled Al-Ca-O sorbents. As Figure 3d–f shows, the 3Al-10Ca-O-nanofibers sorbent that had a 3:10 atomic ratio of Al:Ca had considerably smaller domain sizes, less agglomerated particles, and a more intact porous, fibrous structure than the 1Al-20Ca-O-nanofibers sorbent. The SEM images demonstrate that the

amount of aluminum present in the sorbent affects the degree and speed of collapse of the fibrous structure (particularly, the macropores) upon cycling. The results in this section are in agreement with previous studies on doped or modified sorbents,^[15,23–26,45–47] as it shows that certain inert materials such as $\text{Ca}_{12}\text{Al}_{14}\text{O}_{33}$ can be introduced into the CaO structure to act as a spacer or a physical barrier (thus preventing small CaCO_3 grains from sintering and aggregating) and preserve morphology. Certainly, the combination of metal doping with electrospinning yields a promising avenue and a powerful tool for synthesizing sorbent materials with enhanced sorption capacity for CO_2 removal at elevated temperatures and improved lifespan and stability (i.e., slower decay in the initial sorption capacity).

2.6. CaO-Based Nanofibers in SE-SMR Reactors

1Al-20Ca-O-nanofibers, CaO-nanofibers, CaO-D-acetate, and CaO-marble were tested as sorbents in SE-SMR, and the results are shown in **Figure 8**. SE-SMR was operated under the following reaction conditions: 823 K, 101 kPa total pressure (91 kPa of steam, 28 kPa of methane, and 3 kPa of argon) in a fixed-bed reactor with a commercial NiO-based catalyst (see Experimental Section for details). Initial methane conversion and H_2 product

selectivity (i.e., before complete consumption of the sorbent), defined as moles H_2 per moles total product, and CO_2 breakthrough time (an indicator of sorbent capacity) are shown in **Figure 8a** for the four sorbents tested. Breakthrough time is taken as the data point where the composition of CO_2 equals or exceeds a mole fraction of 0.01. **Figure 8b** shows CO_2 mole fractions in SE-SMR reactor effluents as a function of reaction time on stream (normalized by the space velocity). At early times on stream, undetectable amounts of CO_2 appear in the effluent from the reactor, indicating high rates of sorption (i.e., all CO_2 produced from methane reforming is trapped by the solid CaO). During this stage of the reaction, each reactor (containing 1Al-20Ca-O-nanofibers, CaO-nanofibers, CaO-D-acetate, or CaO-marble) exhibited 100% selectivity to H_2 . After breakthrough, the concentration of CO_2 in the effluent (and correspondingly, the selectivity to H_2 and conversion of methane) approached the SMR equilibrium values (red line in **Figure 8b**). The reactors that contained electrospun materials or CaO-D-acetate approached SMR equilibrium at a slower rate than CaO-marble. This behavior reflects the higher effective diffusivities for these materials (as shown in **Table 3**), which allow nanofiber materials and CaO-D-acetate to continue to adsorb CO_2 at a higher rate than CaO-marble during diffusion-controlled sorption regimes.

As shown in **Figure 8a**, the reactors loaded with the CaO-D-acetate and electrospun materials had a considerably higher methane conversion (88%, 83%, and 84% for CaO-D-acetate, CaO-nanofibers, and 1Al-20Ca-O-nanofibers, respectively) compared with CaO-marble (71%). Each of these systems approaches the same conversion by increasing or decreasing the loading/length (sorbents and catalysts) inside the reactor so that the reactor will always have a low concentration of CO_2 , thereby shifting the SMR reactions toward H_2 products. **Figure 8a** also shows the CO_2 breakthrough time of the three sorbents, which are 1650, 6530, 7500, and 6400 mL g $_{\text{CaO}}^{-1}$ for CaO-marble, CaO-D-acetate, CaO-nanofibers, and 1Al-20Ca-O-nanofibers, respectively. The longer duration of SE-SMR for the electrospun sorbents results primarily from the higher CO_2 capacity of these materials, which is imparted by their smaller CaO crystallite size and larger extent of macroporosity. Their superior performance, as evident in **Figure 7**, impacts the entire SE-SMR process by allowing for a factor of three or more decrease in contact time compared with CaO-marble to produce similar quality hydrogen streams under the same operating conditions (i.e., temperature, pressure, feed composition, and time between regeneration). Alternatively, the nanofibers allow for three or more times longer reaction periods (before regeneration) compared with CaO-marble while producing the same hydrogen stream at the same conditions. Finally, the nanofibers allow for the same quality hydrogen stream to be produced compared with CaO-marble but at milder conditions (i.e., lower temperature and pressures and shorter reactor contact time). Operation at milder conditions decreases capital and operational costs for SE-SMR by allowing for the use of less expensive materials for construction.^[5]

CaO-D-acetate, CaO-nanofibers, and 1Al-20Ca-O-nanofibers were also tested in cyclic SE-SMR/regeneration experiments under the same conditions described in the previous section. After each SE-SMR run, the sorbent was regenerated by flowing

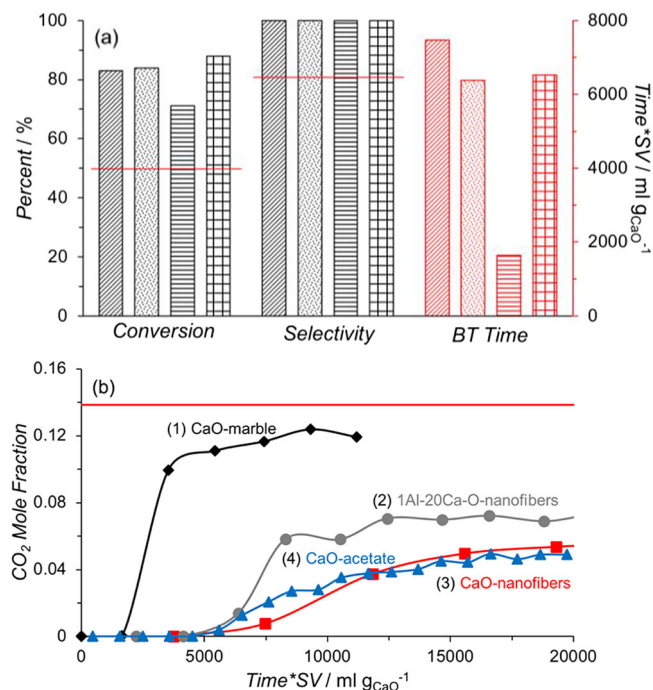


Figure 8. a) Hydrogen selectivity, methane conversion, and CO_2 breakthrough time (BT; red bars) for SE-SMR processes using CaO-marble (horizontal line bars), CaO-D-acetate (squares), CaO-nanofibers (diagonal line bars), and 1Al-20Ca-O-nanofibers (dotted bars). b) CO_2 mole fraction in reactor effluents as a function of time on stream (normalized by space velocity) for SE-SMR experiments using 1) CaO-marble, 2) 1Al-20Ca-O-nanofibers, 3) CaO-nanofibers, and 4) CaO-D-acetate. SMR equilibrium conversion and selectivity (red horizontal lines in (a) and equilibrium CO_2 mole fractions [red line in (b)] are for 823 K. SE-SMR reactions were carried out at 823 K, 91 kPa of steam, 28 kPa of methane, and 3 kPa of argon (total pressure of 101 kPa).

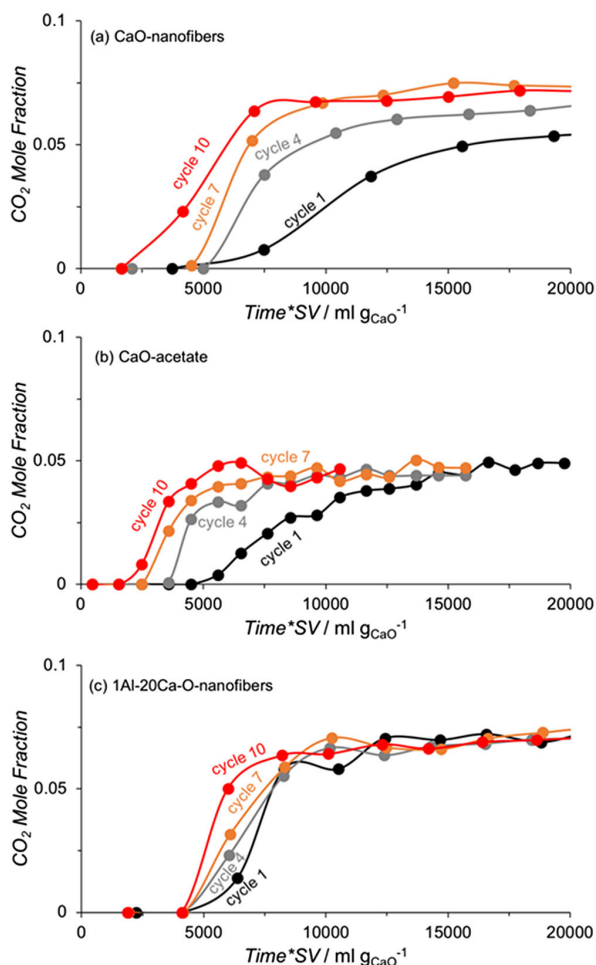


Figure 9. CO₂ mole fraction as a function of time (normalized by space velocity) over ten cycles of SE-SMR/calcination for a) CaO-nanofibers, b) CaO-D-acetate, and c) 1Al-20Ca-O-nanofibers. The data are simplified to show the first run (black), fourth run (grey), seventh run (orange), and tenth run (red).

50 sccm of UHP hydrogen gas at 998 K with a ramping rate of 2 K min⁻¹ and held overnight. The results of these experiments are shown in **Figure 9**. After ten cycles of SE-SMR-regeneration, the CO₂ breakthrough time from reactors containing CaO-D-acetate and CaO-nanofibers decreased by 62% (from 6530 to 2490 mL g_{CaO}⁻¹) and 45% (from 7500 to 4125 mL g_{CaO}⁻¹), respectively, whereas the CO₂ breakthrough time from reactors containing 1Al-20Ca-O-nanofibers decreased by 6% (from 6400 to 6000 mL g_{sorbent}⁻¹), thus indicating better stability during repeated reforming-regeneration cycles, in agreement with results from TGA studies. The high stability of 1Al-20Ca-O nanofibers in SE-SMR agrees with previous studies using nickel supported on Al-Ca-O mixtures.^[27]

3. Conclusions

CaO-based nanofibers (pure CaO and Al-doped) were successfully synthesized via electrospinning and tested for CO₂

sorption capacity and kinetics. Electrospinning, as a synthesis technique, resulted in the fabrication of a connected network of CaO (or Al-Ca-O) nanoparticles, which had a unique, highly porous fibrous structure. The synthesized metal oxide nanofibers were small in size and had large pore volumes, high surface areas, and large intraparticle void spaces. In this work, it was shown that combining electrospinning with metal oxide synthesis resulted in the production of nanostructures that had superior morphologies and physiochemical properties for CaO carbonation compared with the other materials studied.

When reacted with CO₂, electrospun CaO-nanofibers exhibited the highest conversion of all the materials tested, reaching 100% conversion to CaCO₃ (0.79 g_{CO₂} g_{CaO}⁻¹) and exhibiting the highest rate of carbonation of all the materials studied. The saturation capacity of CaO-based sorbents was found to be strongly influenced by properties such as surface area, pore volume, porosity, intraparticle void volume, crystallite size, grain size, and chemical composition. Significant differences in sorption capacities were also observed in CaO-nanofibers, CaO-D-acetate, and CaO-H-nitrate despite similarities in the surface area, pore volume, and crystallite size. The differences in the sorption capacities of these materials were attributed to chemical differences at the reaction interface as well as properties such as pore volume/area and intraparticle void volume.

Aluminum was also studied as a dopant to mitigate the loss of CO₂ capacity over repeated reaction-regeneration cycles. Three Al-doped samples (3Al-10Ca-O-nanofibers, 1Al-10Ca-O-nanofibers, and 1Al-20Ca-O-nanofibers) were tested via TGA and were found to have high sorption capacities (0.35–0.74 g_{CO₂} g_{sorbent}⁻¹). These doped sorbents also demonstrated improved stability (i.e., losing less than 5% of their initial capacity after more than 15 cycles of carbonation-calcination) over CaO-nanofibers, which lost 31% of its initial capacity after 10 cycles, and CaO-marble, which lost 34% of its initial capacity after 10 cycles. This improved performance was due to the presence of stable Al-Ca mixed phases in the sorbent's matrix, which were responsible for retaining the porous, fibrous structure imparted by electrospinning, while also preventing the sorbent's crystallite size from increasing upon cycling. Indeed, the incorporation of aluminum into the CaO matrix is necessary for retaining and mitigating loss in activity.

The improvements observed in the TGA experiments for the electrospun materials were also observed in the SE-SMR reactors where CaO-nanofibers and 1Al-20Ca-O-nanofibers exhibited three or more times longer breakthrough times in SE-SMR than CaO-marble. On multiple SE-SMR/regeneration cycling, the 1Al-20Ca-O-nanofibers showed a superior stability over CaO-nanofibers, losing merely 6% of its breakthrough time after 10 cycles compared with a 45% loss for CaO-nanofibers. The results in this article demonstrate the advantage of using electrospinning as a synthesis approach to producing fibrous structures, with a considerable macroporosity, to enable CaO to reach full conversion to CaCO₃ upon reaction with CO₂. The doping of electrospun CaO-based sorbents with Al and thermally treating the fibers appropriately lead to the formation of high-performing and durable sorbents, which combine the high sorption capacity of electrospun materials and the stability of Al-doped structures.

4. Experimental Section

Materials: PVP (MW 1 300 000, Sigma Aldrich), calcium nitrate tetrahydrate (Sigma Aldrich, $\geq 99.0\%$), calcium acetate hydrate (Alfa Aesar, 99.9965%), CaO from marble (Millipore Sigma), aluminum nitrate nanohydrate (Sigma Aldrich, 99.997%), poly(ethylene glycol)-*block*-poly(propylene glycol)-*block*-poly(ethylene glycol) (P123; Sigma Aldrich, $M_n \approx 5800$), and ethyl alcohol (Sigma Aldrich, 100%) were purchased and used without subsequent purification. The CaO sample from marble is denoted as CaO-marble.

CaO-Based Nanofibers Synthesis via Electrospinning: A polymer solution was prepared by dissolving 1.3 g of PVP in 23 cm³ of ethanol. The solution was then vortexed (Fisher Scientific Digital Vortex Mixer) at 2900 rpm for 1 h until the PVP was completely dissolved. The polymer solution was left to settle for 5–10 min, transferred to a beaker, and stirred for 15 min. The metal containing solution was prepared by dissolving 0.98 g of calcium nitrate and an appropriate amount of aluminum nitrate (for the Al-doped materials) in 10 cm³ of deionized (DI) water and stirring the solution for 0.5 h. The Al:Ca atomic ratios for the three Al-doped samples were 3:10, 1:10, and 1:20. The calcium-containing solution was then added dropwise to the polymer-containing solution. The solution was stirred for 0.25 h and then vortexed for 0.5 h at 2900 rpm.

The electrospinning solution was placed in a 10 mL syringe (BD 10 mL syringe with Luer Lok tip) with a hypodermic needle (Monoject Standard 30G \times $\frac{3}{4}$ "). The distance between the tip of the needle and a stainless steel collecting plate, which was covered with an aluminum foil, was 16 inch. A Gamma High Voltage Research ES75 power supply was used to apply 30 kV on the polymer jet, while the polymer solution was extruded through the needle at a rate controlled by a syringe pump (1.0 cm³ h⁻¹; Kent Scientific Genie Plus). Dry air was circulated inside a 3 m³ chamber at 6 cm³ min⁻¹ to control the relative humidity at 19.5 \pm 2%. All electrospinning was carried out at ambient temperature (294 \pm 3 K) and pressure (101 kPa). The collected fibers were thermally treated in air at 923 K for 8 h at a ramping rate of 5 K min⁻¹ to remove the majority of PVP and form CaO. A second thermal treatment was performed on the Al-doped nanofibers to yield a mayenite structure (Ca₁₂Al₁₄O₃₃),^[48,49] a stable calcium-aluminate framework, and CaO. Specifically, the Al-doped fibers were treated in air at 923 K for 5 h at a ramping rate of 5 K min⁻¹ and then at 1173 K for 2 h at a ramping rate of 2 K min⁻¹. The nondoped electrospun CaO sorbents are denoted as CaO-nanofibers, whereas the Al-doped CaO sorbents are denoted as 3Al-10Ca-O-nanofibers, 1Al-10Ca-O-nanofibers, and 1Al-20Ca-O-nanofibers, where the numbers before Ca and Al correspond to the atomic ratio of Al to Ca in the synthesis procedure.

Thermal Syntheses of CaO from Calcium Acetate and Calcium Nitrate: Calcium acetate was crushed and sieved to <200 mesh and then thermally treated in air at 1023 K for 8 h (ramp rate of 5 K min⁻¹) to form CaO (denoted as CaO-D-acetate). Additionally, calcium nitrate was crushed and sieved to <200 mesh and then thermally treated in air at 923 K for 8 h (ramp rate of 5 K min⁻¹) to form CaO (denoted as CaO-D-nitrate).

A porous CaO sample was synthesized according to the method of surfactant-assisted hydrothermal interaction (denoted as CaO-H-nitrate).^[50,51] First, calcium nitrate was heat-treated under air at 1023 K for 8 h (ramp rate of 5 K min⁻¹) to decompose the nitrate group and form CaO. Subsequently, 0.8 g of CaO was mixed in a beaker containing 150 cm³ of DI water and 5 cm³ of ethanol and stirred for 2 h. The CaO solution was then ultrasonically treated for 2 h. The surfactant solution was prepared by dissolving 2.8 g of P123 in 100 cm³ of water while stirring for 2 h. After stirring, the CaO-containing solution was added to the surfactant solution, left stirring for 72 h, and then ultrasonically treated for 4 h. The solution was then transferred to a 1000 cm³ Teflon-lined stainless steel autoclave for hydrothermal treatment at 473 K for 60 h. The solid substance was filtered out and washed with 480 cm³ of DI water and 20 cm³ of ethanol for the removal of the majority of the P123 surfactant. The solid was then dried overnight in a drying oven at 353 K. The as-obtained material was calcium hydroxide (Ca(OH)₂), which was subsequently thermally treated in air from room temperature to 923 K at a ramping rate of 5 K min⁻¹ for the generation of CaO.

Characterization: The synthesized CaO-based sorbents prepared via thermal decomposition, hydrothermal treatment, and electrospinning were characterized using a variety of techniques. Powder XRD patterns were obtained on an X-ray diffractometer (JEOL JDX-3530 and Philips X-Pert) using Cu K α radiation of 1.54 Å to identify the CaO and Ca₁₂Al₁₄O₃₃ phases. The average crystallite sizes were found using Scherrer's formula. Nitrogen adsorption-desorption isotherms were measured at 77 K with a Micrometrics ASAP 2020 Plus system. The Brunauer-Emmett-Teller (BET) surface areas were calculated from the isotherms. The pore size distribution was derived from the adsorption branches of the isotherms using the Barrett-Joyner-Halenda (BJH) model. SEM with EDS (NOVA 230 Nano SEM/EDS) was used to determine the morphology and chemical composition of the sorbents. The mean diameter and size distribution of the electrospun nanofibers were calculated from the SEM micrographs using ImageJ software ($n = 250$; where, n is the number of fibers that were measured and averaged). The FEI Titan 80–300 kV S/TEM was used to carry out the TEM analysis. The TEM samples were prepared by drop casting an ethanolic dispersion of CaO onto a carbon-coated Cu grid.

Carbonation and Methane Reforming Testing: Reaction kinetics and capacities for CaO carbonation were collected via TGA using a PerkinElmer TGA. Alumina crucibles were used to hold the samples. Gas flow rates were set to 200 standard cm³ min⁻¹ to minimize external diffusion from the bulk gas to the sample interface. Heating/reaction occurred in air (dry, CO₂-free), CO₂ (Wright Bros, Inc., 99.5%), and/or argon (Matheson UHP Argon, 99.999% purity) at a ramping rate of 5–20 K min⁻¹. Prior to the carbonation reaction testing, CaO-marble samples were crushed and sieved to <200 mesh. Prior to all reactions (carbonation or methane reforming), all samples were calcined in air at 923 K with a ramp rate of 5 K min⁻¹ for 8 h in a Thermolyne F6028C-80 muffle furnace. In the TGA, prior to reaction with CO₂, the CaO-based sorbents were treated at 1073 K for 10 min at a ramp rate of 10 K min⁻¹ in air to ensure the decomposition of any residual Ca(OH)₂ or CaCO₃ that formed during the exposure to the atmosphere.^[19] After the in situ calcination, the samples were cooled at a rate of 20 K min⁻¹ to their reaction temperatures and held for 20 min to equilibrate. All samples were carbonated for 1 h at 101 kPa in 200 sccm of pure CO₂.

The first cycle for each of the cycling studies was carried out according to the methods described in the previous paragraph. For subsequent cycles, following 1 h of carbonation, the gas was switched from CO₂ to air, and the temperature was ramped from 873 to 1073 K at a rate of 10 K min⁻¹. Samples were held at 1073 K for 10 min and then cooled to 873 K at a rate of 15 K min⁻¹. Samples were then held at 873 K for 15 min to equilibrate before the gas was switched from air to CO₂ to begin subsequent carbonation.

CaO-marble, CaO-nanofibers, and 1Al-20Ca-O-nanofibers were tested for SE-SMR in a stainless steel packed bed reactor ($\frac{1}{2}$ inch OD) containing physical mixtures of commercial NiO-based methane reforming catalyst (HiFUEL R110, Alfa Aesar, 40% nickel (II) oxide and 60% aluminum oxide) with CaO-marble (2.58 g of CaO-marble with 1.01 g of HiFUEL; 180–250 μ m particles), CaO-D-acetate (0.660 g CaO-D-acetate with 1.42 g HiFUEL), CaO-nanofibers (0.247 g CaO-nanofibers with 0.384 g HiFUEL), or 1Al-20Ca-O-nanofibers (0.322 g 1Ca-20Al-O-nanofibers with 0.421 g HiFUEL) between two plugs of quartz wool. The CO₂ sorbents were pretreated ex situ at 923 K for 8 h at a ramp rate of 5 K min⁻¹ in air. Prior to reaction, the sorbent/catalyst mixture was pretreated in situ under 50 sccm H₂ at 998 K (ramp rate of 2.3 K min⁻¹) for 10 h. After the H₂ pretreatment, the temperature was reduced to 823 K (measured with a type-K thermocouple) in 50 sccm helium (Airgas UHP helium, 99.999% purity) before the introduction of a 90% methane/10% argon reactant mixture (Praxair, $\pm 2\%$ methane). Reactant and product compositions were measured online using an Agilent 7890B GC system with a thermal conductivity detector. All gasses were introduced with electronic mass flow controllers (MKS, model GE50A). Water was introduced through a positive displacement pump into the gas line, which was heated to temperatures above 393 K from the gas inlet to the post-reactor condenser to ensure that all water in the system is in the vapor

phase (temperatures along the gas line were measured using type-K thermocouples). The total flow rate at the reaction conditions for the SE-SMR reaction containing CaO-marble was $300 \text{ cm}^{-3} \text{ min}^{-1}$, and for the reaction containing CaO-nanofibers and 1Al-20Ca-O-nanofibers, the total flow rate was $100 \text{ cm}^{-3} \text{ min}^{-1}$. The ratio of sorbent to gas flow was $120 \text{ cm}^{-3} \text{ min}^{-1} \text{ g}^{-1}$ for the reaction containing CaO-marble and $405 \text{ cm}^{-3} \text{ min}^{-1} \text{ g}^{-1}$ and $310 \text{ cm}^{-3} \text{ min}^{-1} \text{ g}^{-1}$ for the reactions containing CaO-nanofibers and 1Al-20Ca-O-nanofibers, respectively. The steam to carbon ratio is 3 for all reactions.

Random Pore Model: The random pore model (RPM), first proposed by Bhatia and Perlmutter^[52,53] and simplified to two equations by Grasa et al.^[54] for the kinetic [Equation (1)] and diffusion reaction regimes [Equation (2)], was used in this work to quantify carbonation reaction kinetics in terms of the reaction rate constant (k_{RPM}) and the effective diffusivity (D_{RPM}). The structural parameter, Ψ [Equation (3)], was calculated using the initial surface area (S_0), initial length of pores (L_0), and initial porosity (ϵ_0), which were determined from the N_2 physisorption isotherms (see Supporting Information for details). The RPM was not applied to the cycling studies due to potential changes in Ψ during carbonation–calcination cycling. In Equation (1) and (2), C_b , C_e , t , M_{CaO} , ρ_{CaO} , and Z are the bulk concentration of CO_2 , equilibrium concentration of CO_2 , reaction time, molar mass of CaO, density of CaO, and ratio of molar volumes of CaCO_3 to CaO, respectively.

$$\frac{1}{\Psi} \left[\sqrt{1 - \Psi \ln(1 - X)} - 1 \right] = \frac{k_{\text{RPM}} S_0 (C_b - C_e) t}{2(1 - \epsilon_0)} \quad (1)$$

$$\frac{1}{\Psi} \left[\sqrt{1 - \Psi \ln(1 - X)} - 1 \right] = \frac{S_0}{(1 - \epsilon_0)} \sqrt{\frac{D_{\text{RPM}} M_{\text{CaO}} C_b t}{2\rho_{\text{CaO}} Z}} \quad (2)$$

$$\Psi = \frac{4\pi L_0 (1 - \epsilon_0)}{S_0^2} \quad (3)$$

Supporting Information

Supporting Information is available from the Wiley Online Library or from the author.

Acknowledgements

F.H.A. and L.T.M. contributed equally to this work. The authors acknowledge the financial support from Henry Samueli School of Engineering and Applied Sciences and the Office of Equity, Diversity, and Inclusion at UCLA. The authors also acknowledge the Molecular & Nano Archaeology (MNA) Laboratory at UCLA Materials Science Department for use of the SEM, the J.D. McCullough Laboratory of X-ray Crystallography at UCLA Chemistry Department for use of the XRD, the Molecular Instrumentation Center (MIC) at UCLA for use of the TGA, and California NanoSystems Institute (CNSI) at UCLA for use of the TEM. The authors acknowledge Sara Azzam for assistance with XRD and Zubin Mishra and Richa Ghosh for assistance with conducting the electrospinning experiments. F.H.A. acknowledges Aramco R&D for supporting his graduate studies at UCLA.

Conflict of Interest

The authors declare no conflict of interest.

Keywords

calcium oxide, carbonation, electrospinning, green hydrogen, natural gas reforming, sorption enhanced processes

Received: September 6, 2018

Revised: November 28, 2018

Published online:

- [1] H. Lu, A. Khan, P. G. Smirniotis, *Ind. Eng. Chem. Res.* **2008**, *47*, 6216.
- [2] J. Yu, L.-H. Xie, J.-R. Li, Y. Ma, J. M. Seminario, P. B. Balbuena, *Chem. Rev.* **2017**, *117*, 9674.
- [3] G. T. Rochelle, *Science* **2009**, *325*, 1652.
- [4] D. Y. C. Leung, G. Caramanna, M. M. Maroto-Valer, *Renewable Sustainable Energy Rev.* **2014**, *39*, 426.
- [5] D. P. Harrison, *Ind. Eng. Chem. Res.* **2008**, *47*, 6486.
- [6] S.-Y. Lin, Y. Suzuki, H. Hatano, M. Harada, *Energy Fuels* **2001**, *15*, 339.
- [7] A. Lopez Ortiz, D. P. Harrison, *Ind. Eng. Chem. Res.* **2001**, *40*, 5102.
- [8] N. Chanburanasiri, A. M. Ribeiro, A. E. Rodrigues, A. Arpornwichanop, N. Laosiripojana, P. Praserttham, S. Assabumrungrat, *Ind. Eng. Chem. Res.* **2011**, *50*, 13662.
- [9] C. S. Martavaltzi, E. P. Pampaka, E. S. Korkakaki, A. A. Lemonidou, *Energy Fuels* **2010**, *24*, 2589.
- [10] M. Ramezani, P. Tremain, E. Doroodchi, B. Moghtaderi, *Energy Procedia* **2017**, *114*, 259.
- [11] H. Guo, S. Wang, C. Li, Y. Zhao, Q. Sun, X. Ma, *Ind. Eng. Chem. Res.* **2016**, *55*, 7873.
- [12] C. Luo, Y. Zheng, J. Guo, B. Feng, *Fuel* **2014**, *127*, 124.
- [13] J. Blamey, E. J. Anthony, J. Wang, P. S. Fennell, *Prog. Energy Combust. Sci.* **2010**, *36*, 260.
- [14] S. M. M. Nouri, H. A. Ebrahim, *Braz. J. Chem. Eng.* **2016**, *33*, 383.
- [15] W. Liu, H. An, C. Qin, J. Yin, G. Wang, B. Feng, M. Xu, *Energy Fuels* **2012**, *26*, 2751.
- [16] G. S. Grasa, J. C. Abanades, *Ind. Eng. Chem. Res.* **2006**, *45*, 8846.
- [17] B. R. Stanmore, P. Gilot, *Fuel Process. Technol.* **2005**, *86*, 1707.
- [18] S. Kumar, S. K. Saxena, *Mater. Renew. Sustain. Energy* **2014**, *3*, 30.
- [19] H. Lu, E. P. Reddy, P. G. Smirniotis, *Ind. Eng. Chem. Res.* **2006**, *45*, 3944.
- [20] H. Lu, A. Khan, S. E. Pratsinis, P. G. Smirniotis, *Energy Fuels* **2009**, *23*, 1093.
- [21] R. Koirala, K. R. Gunugunuri, S. E. Pratsinis, P. G. Smirniotis, *J. Phys. Chem. C* **2011**, *115*, 24804.
- [22] L. Zhang, B. Zhang, Z. Yang, M. Guo, *Energy Technol.* **2015**, *3*, 10.
- [23] C. S. Martavaltzi, A. A. Lemonidou, *Microporous Mesoporous Mater.* **2008**, *110*, 119.
- [24] C. S. Martavaltzi, A. A. Lemonidou, *Ind. Eng. Chem. Res.* **2008**, *47*, 9537.
- [25] I. Aloisi, A. Di Giuliano, A. Di Carlo, P. U. Foscolo, C. Courson, K. Gallucci, *Chem. Eng. J.* **2017**, *314*, 570.
- [26] A. Di Giuliano, J. Girr, R. Massacesi, K. Gallucci, C. Courson, *Int. J. Hydrogen Energy* **2017**, *42*, 13661.
- [27] A. Di Giuliano, K. Gallucci, F. Giancaterino, C. Courson, P. U. Foscolo, *Chem. Eng. J.* **2018**, DOI: 10.1016/j.cej.2018.09.035.
- [28] M. L. Granados, M. D. Z. Poves, D. M. Alonso, R. Mariscal, F. C. Galisteo, R. Moreno-Tost, J. Santamaría, J. L. G. Fierro, *Appl. Catal., B* **2007**, *73*, 317.
- [29] Z. Li, N. Cai, Y. Huang, *Ind. Eng. Chem. Res.* **2006**, *45*, 1911.
- [30] M. M. Hohman, M. Shin, G. Rutledge, M. P. Brenner, *Phys. Fluids* **2001**, *13*, 2221.
- [31] Y. M. Shin, M. M. Hohman, M. P. Brenner, G. C. Rutledge, *Polymer (Guildf)* **2001**, *42*, 9955.
- [32] J. Piella, F. Merkoci, A. Genc, J. Arbiol, N. G. Bastus, V. Puntes, *J. Mater. Chem. A* **2017**, *5*, 11917.
- [33] V. Beachley, X. Wen, *Mater. Sci. Eng., C* **2009**, *29*, 663.
- [34] X.-H. Qin, E.-L. Yang, N. Li, S.-Y. Wang, *J. Appl. Polym. Sci.* **2006**, *103*, 3865.
- [35] W. Liu, N. W. L. Low, B. Feng, G. Wang, J. C. Diniz da Costa, *Environ. Sci. Technol.* **2010**, *44*, 841.

- [36] H. Gupta, L.-S. Fan, *Ind. Eng. Chem. Res.* **2002**, *41*, 4035.
- [37] Z. Zhou, P. Xu, M. Xie, Z. Cheng, W. Yuan, *Chem. Eng. Sci.* **2013**, *95*, 283.
- [38] M. Chen, D. W. Goodman, *Catal. Today* **2006**, *111*, 22.
- [39] A. T. Bell, *Science* **2003**, *299*, 1688.
- [40] G. A. Somorjai, *Science* **1985**, *227*, 902.
- [41] D. Mess, A. F. Sarofim, J. P. Longwell, *Energy Fuels* **1999**, *13*, 999.
- [42] Z. Li, M. Flytzani-Stephanopoulos, *Ind. Eng. Chem. Res.* **1997**, *36*, 187.
- [43] R. Barker, *J. Appl. Chem. Biotechnol.* **1974**, *24*, 221.
- [44] M. V. Iyer, H. Gupta, B. B. Sakadjian, L.-S. Fan, *Ind. Eng. Chem. Res.* **2004**, *43*, 3939.
- [45] J. M. López, M. V. Navarro, R. Murillo, G. S. Grasa, *Energy Procedia* **2017**, *114*, 230.
- [46] C. Luo, Y. Zheng, N. Ding, Q. Wu, G. Bian, C. Zheng, *Ind. Eng. Chem. Res.* **2010**, *49*, 11778.
- [47] A. M. Kierzkowska, R. Pacciani, C. R. Müller, *ChemSusChem* **2013**, *6*, 1130.
- [48] H. Boysen, M. Lerch, A. Stys, A. Senyshyn, *Acta Crystallogr., Sect. B: Struct. Sci., Cryst. Eng. Mater.* **2007**, *63*, 675.
- [49] S. S. Kazi, A. Aranda, J. Meyer, J. Mastin, *Energy Procedia* **2014**, *63*, 2207.
- [50] C. Liu, L. Zhang, J. Deng, Q. Mu, H. Dai, H. He, *J. Phys. Chem. C* **2008**, *112*, 19248.
- [51] J. C. Yu, A. Xu, L. Zhang, R. Song, L. Wu, *J. Phys. Chem. B* **2004**, *108*, 64.
- [52] S. K. Bhatia, D. D. Perlmutter, *AIChE J.* **1980**, *26*, 379.
- [53] S. K. Bhatia, D. D. Perlmutter, *AIChE J.* **1981**, *27*, 247.
- [54] G. Grasa, R. Murillo, M. Alonso, J. C. Abanades, *AIChE J.* **2009**, *55*, 1246.